

Imaging a light-induced molecular elimination reaction with an X-ray free-electron laser

Received: 6 April 2025

Accepted: 16 July 2025

Published online: 30 July 2025

Check for updates

Xiang Li¹✉, Rebecca Boll², Patricia Vindel-Zandbergen³, Jesús González-Vázquez⁴, Daniel E. Rivas², Surjendu Bhattacharyya⁵, Kurtis Borne⁵, Keyu Chen⁵, Alberto De Fanis², Benjamin Erk⁶, Ruairidh Forbes^{1,7,8}, Alice E. Green^{2,7,9}, Markus Ilchen^{2,6,10}, Balram Kaderiya⁵, Edwin Kukk¹¹, Huynh Van Sa Lam⁵, Tommaso Mazza², Terence Mullins^{2,6,12}, Björn Senfftleben², Florian Trinter^{13,14}, Sergey Usenko², Anbu Selvam Venkatachalam⁵, Enliang Wang⁵, James P. Cryan^{1,7}, Michael Meyer², Till Jahnke^{2,15}, Phay J. Ho¹⁶, Daniel Rolles⁵ & Artem Rudenko⁵✉

Tracking the motion of individual atoms during chemical reactions represents a severe experimental challenge, especially if several competing reaction pathways exist or if the reaction is governed by the correlated motion of more than two molecular constituents. Here we demonstrate how ultrashort X-ray pulses combined with coincident ion imaging can be used to trace molecular iodine elimination from laser-irradiated diiodomethane (CH₂I₂), a reaction channel of fundamental importance but small relative yield that involves the breaking of two molecular bonds and the formation of a new one. We map bending vibrations of the bound molecule, disentangle different dissociation pathways, image the correlated motion of the iodine atoms and the methylene group leading to molecular iodine ejection, and trace the vibrational motion of the formed product. Our results provide a quantitative mechanistic picture behind previously suggested reaction mechanisms and prove that a variety of geometries are involved in the molecular bond formation.

Elimination reactions are an important class of chemical processes in which a pair of atoms or two groups of atoms are removed from a reactant to form a new product¹. Most elimination reactions involve the formation of a new bond, and often result in the ejection of a small molecule like water, hydrogen, or hydrogen halides^{2,3}. Such

reactions can proceed via concerted or stepwise mechanisms^{1–3} and typically require a coordinated motion of several atoms involved in multiple bonds breaking and forming. With the development of femtosecond techniques that provide a time-domain view of molecular processes^{4,5}, elimination reactions attracted particular

¹Linac Coherent Light Source, SLAC National Accelerator Laboratory, Menlo Park, CA, USA. ²European XFEL, Holzkoppel 4, Schenefeld, Germany.

³Department of Chemistry, New York University, New York, NY, USA. ⁴Departamento de Química, Universidad Autónoma de Madrid, Cantoblanco, Madrid, Spain. ⁵J.R. Macdonald Laboratory, Department of Physics, Kansas State University, Manhattan, KS, USA. ⁶Deutsches Elektronen-Synchrotron (DESY), Notkestrasse 85, Hamburg, Germany. ⁷Stanford PULSE Institute, SLAC National Accelerator Laboratory, Menlo Park, CA, USA. ⁸Department of Chemistry, University of California, Davis, CA, USA. ⁹EaStCHEM School of Chemistry, University of Edinburgh, Edinburgh, UK. ¹⁰Department of Physics, University of Hamburg, Hamburg, Germany. ¹¹Department of Physics and Astronomy, University of Turku, Turku, Finland. ¹²The Hamburg Centre for Ultrafast Imaging, Universität Hamburg, Hamburg, Germany. ¹³Molecular Physics, Fritz-Haber-Institut der Max-Planck-Gesellschaft, Berlin, Germany. ¹⁴Institut für Kernphysik, Goethe-Universität Frankfurt, Frankfurt am Main, Germany. ¹⁵Max-Planck-Institut für Kernphysik, Heidelberg, Germany. ¹⁶Chemical Sciences and Engineering Division, Argonne National Laboratory, Lemont, IL, USA. ✉ e-mail: xiangli@slac.stanford.edu; rudenko@ksu.edu

attention because they often involve different dynamics leading to the same final products^{6–14}.

One of the most extensively studied reactions of this type is the light-induced elimination of molecular halogens from halomethanes^{9–20}. Such photolysis processes in halomethanes are important because of their relevance in atmospheric chemistry and, in particular, because of their suggested role in the catalytic ozone layer depletion^{21,22}. Depending on the wavelength and the intensity of the light driving the reaction, they can happen in either the neutral or the ionic state and can eliminate a neutral halogen molecule^{9–14,16–18} or a molecular ion^{15,19,20}. The products of such reactions have been characterized by mass spectrometry^{15,19}, fluorescence detection^{9–14}, or transient absorption²⁰. All of these studies led to the conclusion that the elimination of a molecular halogen proceeds in a concerted manner. More specifically, two different concerted scenarios, termed “synchronous” and “asynchronous”, have been suggested, implying symmetric and asymmetric geometries, respectively, at the time of molecular halogen formation^{9–16}. For the microscopic understanding of the actual reaction mechanism, it would be crucial to trace the motion of individual atoms leading to the formation of the halogen molecule, whose timescale is comparable to the molecular vibrations. These initial steps are, however, difficult to disentangle from the motion of the bound molecule and from contributions of various competing dissociation pathways. In particular for diffraction-based techniques such as ultrafast electron diffraction^{7,23,24} and X-ray scattering²⁵, the characterization of such elimination reactions is challenging if the distance between the two strongly scattering halogen atoms in the product and reactant are identical. Moreover, diffraction-based techniques probe the entire ensemble of target molecules and, as such, are most sensitive to the major reaction channel(s), especially for dilute gas-phase targets.

Here we report on imaging of molecular iodine elimination from laser-ionized diiodomethane (CH_2I_2) in the gas phase employing Coulomb explosion by intense femtosecond X-ray pulses. Because of its rich photoinduced dynamics and its atmospheric relevance, diiodomethane has been recently studied in various time-resolved experiments employing ultrafast electron diffraction²⁴, photoelectron spectroscopy^{24,26}, ultrafast X-ray scattering^{27,28}, extreme-ultraviolet transient absorption^{20,29}, and ion momentum spectroscopy^{30,31}. By combining coincident Coulomb explosion imaging (CEI)^{32–35} with element-specific X-ray ionization, we disentangle the signatures of molecular halogen formation from competing dynamical processes including the vibrational motion of the bound molecule and all other dissociation pathways involving cleavage of one or both iodine-carbon bonds. Our data show that the iodine molecule (most often ejected as a singly charged molecular ion) is formed at a broad range of internuclear separations, corresponding to a variety of bound and metastable excited states. We trace the vibrational motion of the formed I_2^+ molecule and show that both “synchronous” and “asynchronous” mechanisms contribute to its formation. While the motion of molecular constituents during the bond formation and subsequent vibrations of the formed product have recently been mapped by X-ray scattering in solution (using the $[\text{AuCN}_2^-]$ trimer as an example)³⁶, to the best of our knowledge, such mapping has not been demonstrated for the motion of individual atoms in a gas-phase reaction. Our results provide the long sought-after mechanistic picture of the rich light-induced structural dynamics in diiodomethane and presents an efficient scheme for identifying and disentangling several competing interweaved reaction pathways—a common challenge for all ultrafast molecular imaging techniques.

Results and discussion

The experiment, schematically illustrated in Fig. 1a, was performed using the COLTRIMS (COLD Target Recoil Ion Momentum Spectroscopy) reaction microscope^{37,38} at the Small Quantum Systems (SQS) scientific instrument at the European X-ray Free-Electron Laser

(EuXFEL). Intense ($\sim 1 \times 10^{14} \text{ W/cm}^2$) near-infrared (NIR) laser pulses were used to irradiate CH_2I_2 molecules delivered as a dilute supersonic molecular beam, triggering the reactions of interest. The reaction dynamics were probed via multiple ionization and subsequent rapid fragmentation (Coulomb explosion) of the molecules by intense 2-keV X-ray pulses arriving at variable time delays with respect to the NIR pump pulse. We analyzed four or five ionic fragments detected in coincidence for each fragmentation event and reconstructed their three-dimensional (3D) molecular-frame momentum distributions (MFMDs) following the analysis approach introduced in ref. 35. The MFMD obtained with only the X-ray pulse is shown in Fig. 1b, for fragmentation into the final charge-state combination $\text{C}^+/\text{I}^+/\text{I}^{5+}/\text{H}^+/\text{H}^+$ (in the following, we omit H^+ from the notation). The 3D pattern shows a structure that can be associated with the equilibrium geometry of the molecule (shown in the inset), reflecting its C_{2v} symmetry, and mapping all five molecular constituents into localized spots in momentum space. The MFMDs for other charge-state combinations obtained with only the X-ray pulse are qualitatively similar, see Supplementary Fig. 1a–c.

Figure 1c shows the MFMD for the same coincidence channel at a pump-probe delay of 500 fs. Compared to the data for unpumped molecules (Fig. 1b), in addition to the localized spots, it displays a broader structure for the iodine ions. This broad structure in momentum space corresponds to ions with low kinetic energies (Supplementary Fig. 1i), suggesting that it originates from molecules with larger interatomic distances (and thus, weaker electrostatic repulsion)—i.e., those dissociated by the pump pulse³⁹. Remarkably, the appearance and shape of this additional structure depends on the particular charge-state combination selected (Fig. S1e–g). We find that these differences between the observed pump-probe patterns for different channels reflect the fact that certain charge-state combinations produced by the X-ray probe strongly favor particular molecular configurations created by the NIR pump pulse, thus effectively selecting specific pump-induced dynamics (see Supplementary Table 1a and Section 2 of Supplementary Discussion for details on the reaction pathway selectivity of different charge-state combinations).

In the following, we will exploit this pathway selectivity to study molecular iodine elimination by focusing on the $\text{C}^+/\text{I}^+/\text{I}^{5+}$ final state. The production of such ion fragment combinations, with low carbon charge state and high charge states of both iodines, is favored if the NIR pulse triggers I_2 or I_2^+ ejection because at 2 keV, X-ray ionization is predominantly localized at the iodine sites and charge transfer to carbon is suppressed due to the increased C-I distances⁴⁰. Therefore, this channel contains a significant fraction of events resulting from the elimination reaction of interest, which helps to disentangle it from competing, more probable processes triggered by the NIR pump pulse. Since the NIR-induced dynamics at the intensity used in this work are dominated by the cationic states^{15,19,20}, a reasonable estimate of the branching ratios of different reaction pathways can be obtained from the NIR-only measurement. As shown in Supplementary Table 1b, the pathways involving molecular iodine formation (mainly I_2^+) constitute only ~10% of the total ionization and fragmentation yield generated by the NIR pulse, whereas the majority of the fragments are due to the events where molecules remained bound or only one of the two C-I bonds was cleaved.

To separate the events involving I_2 or I_2^+ formation from the contributions resulting from competing pathways, we consider the delay-dependent kinetic energy distributions (KEDs) of C^+ ions from the $\text{C}^+/\text{I}^+/\text{I}^{5+}$ channel in Fig. 2a. Molecular iodine elimination requires both C-I bonds to break, thus resulting in a large separation between the iodine atoms and the methylene group at the time when the X-ray probe pulse arrives. This should lead to a low kinetic energy (KE) of the carbon ion after Coulomb explosion for long pump-probe delays³⁹. Indeed, the KED of the C^+ ions in Fig. 2a clearly displays a corresponding feature, which descends to low KEs (<20 eV) at large delays.

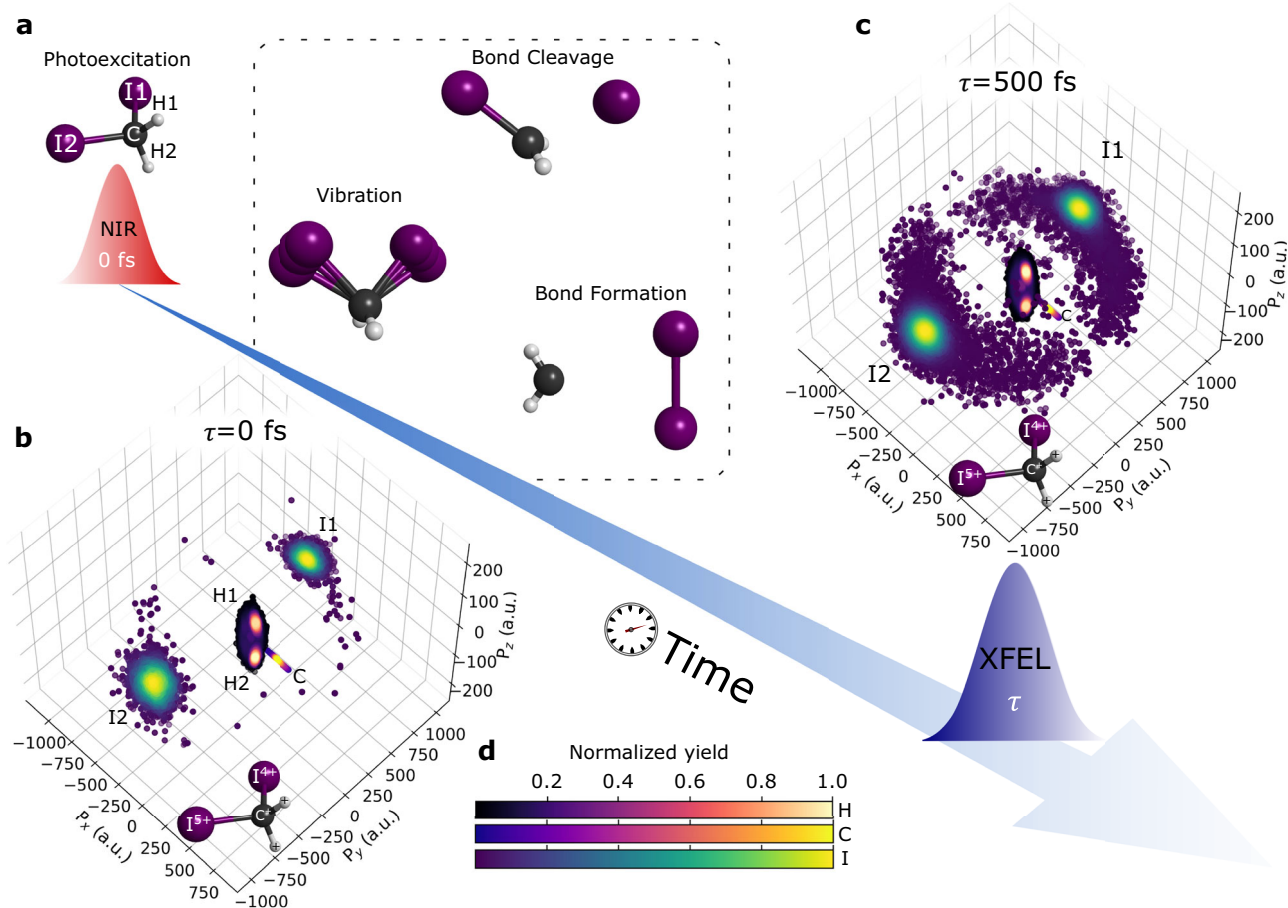


Fig. 1 | Experiment sketch and molecular-frame momentum distributions of ions from X-ray ionization of laser-excited CH_2I_2 molecules. **a** Illustration of the photoexcitation of a CH_2I_2 molecule by a NIR pulse, possible nuclear dynamics after NIR excitation, and probing by an XFEL pulse arriving after time delay τ . **b, c** Molecular-frame momentum distributions of ion fragments from the C^+/I^{4+}

$\text{I}^{5+}/\text{H}^+/\text{H}^+$ coincidence channel resulting from XFEL ionization of unpumped CH_2I_2 molecules (**b**) and from XFEL ionization of CH_2I_2 molecules 500 fs after the irradiation by an 800-nm NIR laser pulse (**c**). Panels **b** and **c** share the same color bars shown in (**d**).

The distribution also contains a high-KE delay-independent band centered around 45 eV, which results from the Coulomb explosion of bound molecules. While the MFMD (Fig. 2b) for the high-KE band displays two well-localized iodine spots, nearly identical to the static case shown in Fig. 1b, the MFMD (Fig. 2c) for the low-KE band descending as a function of delay shows a smeared-out, ring-like structure corresponding to the additional feature appearing in Fig. 1c due to dissociating events.

The high-energy band in Fig. 2a is formed by the contributions from CH_2I_2 molecules that remained bound after the NIR pump pulse (pumped or unpumped). This is a universal feature appearing in all final charge-state combinations. However, since charge redistribution in bound molecules favors the production of ionic fragments with similar charges, the dominant channel reflecting the bound-state dynamics is found to be $\text{C}^{2+}/\text{I}^{3+}/\text{I}^{3+}$. Note that a significant portion of the NIR-induced ions are bound parent molecules (CH_2I_2^+), as shown in Supplementary Table 1b, which, upon X-ray ionization, produce carbon ions with a kinetic energy similar to that of X-ray ionized neutral molecules. Therefore, the high-energy band includes a significant fraction of molecules that were ionized and vibrationally excited by the NIR pulse. To trace the resulting vibrational wave packet, in Fig. 2d, we use the dominant channel and plot the mean value of the measured momentum-space I-C-I angle $\Delta\text{ICI}^{(M)}$ (illustrated in Fig. 2b). The time-resolved data exhibit a pronounced oscillatory structure with a period of 300 ± 9 fs, which, according to our analysis, reflects the ground-state bending vibration (“scissors” mode) of CH_2I_2^+ ^{19,20}. As shown

earlier, under certain conditions, the measured delay-dependent momentum-space angles can be used to track the evolving real-space angles in a molecule undergoing complex vibrations (e.g., torsional motion)^{41,42}. To quantitatively map the momentum-space measurements to real-space angles, we performed simulations of the X-ray multiphoton-induced Coulomb explosion of molecules with various I-C-I angles, which showed that for CH_2I_2 the calculated momentum-space angle $\Delta\text{ICI}^{(M)}$ decreases with increasing real-space I-C-I angle $\Delta\text{ICI}^{(R)}$ (Supplementary Fig. 2b). The simulated curve, which is based on the expected wave packet motion in the CH_2I_2^+ ground state (grey solid line in Fig. 2d), matches both the amplitude and phase of the experimental data, confirming that the observed oscillation reflects the vibrational motion of the laser-ionized molecule. A more detailed analysis of the wave packet’s phase and angular range supporting the assignment of the observed “scissors” motion to CH_2I_2^+ rather than neutral CH_2I_2 , is presented in Section 3 of Supplementary Discussion and Supplementary Fig. 6.

After characterizing the motion of the bound part of the laser-induced nuclear wave packet, we now focus on events resulting in molecular iodine elimination, which correspond to the low-KE part of Fig. 2a. While the appearance of low-KE C^+ ions is a necessary condition, it is not sufficient for the isolation of I_2^+ formation from other dissociation channels. If I_2^+ is formed, the I-I distance stays essentially constant after the initial formation, except for possible vibrations of the product. Correspondingly, the sum KE of the two iodine ions is expected to converge to a rather high, nearly constant value

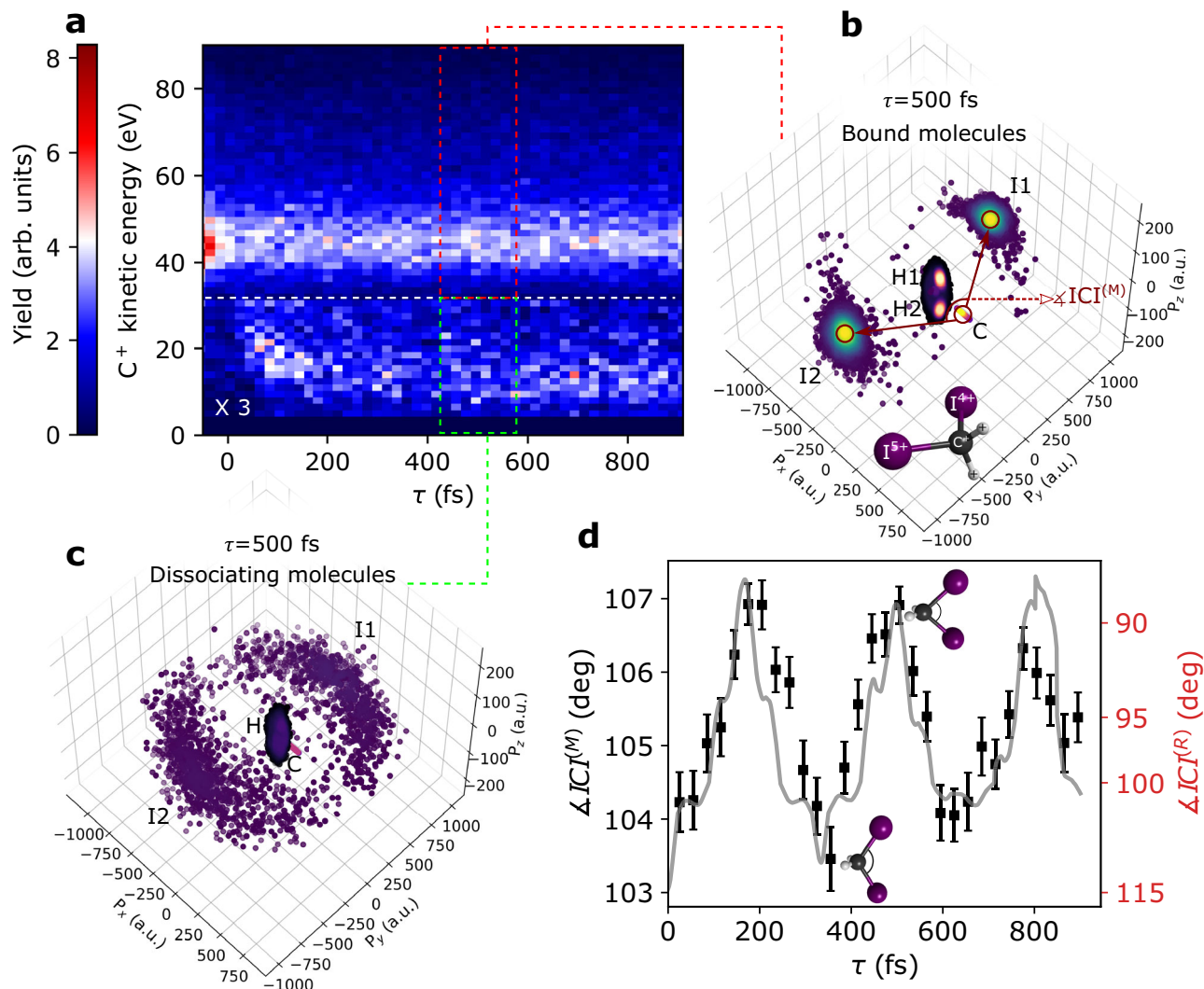


Fig. 2 | Separation of bound and dissociating molecules and imaging of bending vibrations. **a** Time-dependent KED of C^+ ions for the $C^+/I^{3+}/I^{5+}$ channel. The white dashed line marks the boundary (32 eV) used for separating signals from bound and dissociating molecules. The intensity in the region below the white line is scaled by a factor of 3 to increase the visibility of the dissociation channel. **b, c** MFMDs for bound (**b**) and dissociating (**c**) molecules (events within the red and green boxes

centered at 500 fs in **a**). **d** Mean value of the momentum-space I-C-I angle $\Delta ICI^{(M)}$ (defined in red in panel **b**) as a function of NIR/X-ray delay for the $C^{2+}/I^{3+}/I^{5+}$ channel. Squares represent the measured data and the grey solid line the simulated values. The error bars reflect the standard error of the mean. The numbers on the right axis show the values of the real-space angle $\Delta ICI^{(R)}$ corresponding to the simulated $\Delta ICI^{(M)}$ angles.

determined by the I-I bond length. The combined KE of the two iodine fragments is plotted as a function of the delay in Fig. 3a (selecting only the dissociating events with low C^+ KE in Fig. 2a). Even though for the delays larger than -100 fs the carbon fragment clearly moves further away from both iodines, resulting in the smaller Coulomb repulsion, the distribution is dominated by events with high sum KEs. This can only happen for short I-I distances, confirming that the spectrum in Fig. 3a mainly contains events involving I_2^+ (or I_2) formation. Note that the iodine sum KED is qualitatively different for channels where only one C-I bond is broken, and no molecular iodine is formed (see Supplementary Fig. 7).

At small NIR/X-ray delays, the dominant part of the sum KE spectrum initially moves towards lower values, reflecting the rapid detachment of the methylene group. However, from -150–200 fs onwards, the distribution broadens, with the mean shifting back towards higher KE with increasing delay. This behavior maps the reduction of the I-I distance when the molecular iodine is formed. A cartoon of the I_2^+ formation pathways and the corresponding molecular dynamics simulation visualizing the correlated change in the I-I and both C-I distances are shown in Fig. 4a, c. The appearance of a clear

high-energy component, not present in the data for the first 200 fs, is highlighted in Fig. 3b, where the I-I sum KE distributions for 0–200 fs and 600–850 fs are compared. In addition, as can be seen in Fig. 3a, b, a clear feature develops at low energies for larger delay times. This feature reflects events where both C-I bonds and the I-I bond have been broken by the time the probe pulse arrives. The delay dependence of this low-energy part of the spectrum suggests that there are two contributing processes: First, the pump pulse can result in three-body dissociation of the molecule, where the methylene group and the two iodine fragments directly move apart. Second, I_2^+ can be formed in one of highly excited metastable states⁴³, which dissociate into a $I + I^+$ after a certain time following the pump pulse. These dissociating I_2^+ molecules result in the events which drop below the intense horizontal band in Fig. 3a at longer delays since the kinetic energy gained from the Coulomb explosion after X-ray ionization decreases as the internuclear distance between I and I^+ increases.

In order to relate the measured KEs to the internuclear separation, we use Coulomb explosion simulations for various molecular geometries. After validating the simulation for the unpumped CH_2I_2 molecule (see Supplementary Fig. 8), we calculated the sum KED of the I^{4+} and I^{5+}

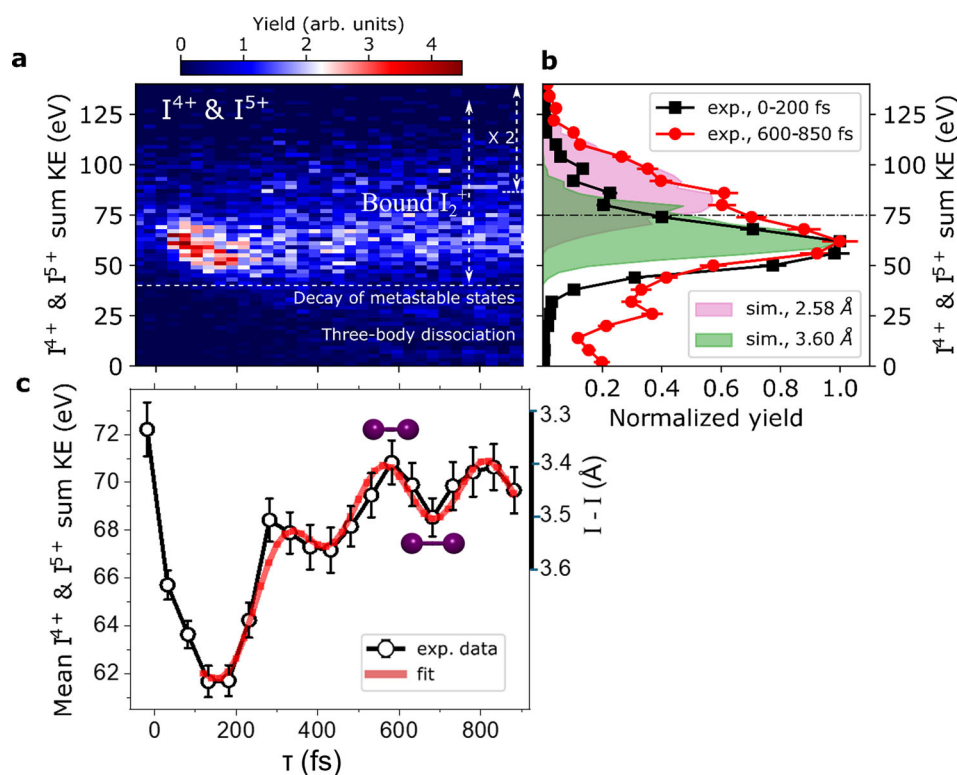


Fig. 3 | Imaging of I_2^+ formation with the $C/I^{4+}/I^{5+}$ coincidence channel. **a Time-dependent sum KED of I^{4+} and I^{5+} for the events below the white line in Fig. 2a. The horizontal white dashed line in **a** shows the lower limit (40 eV) of I^{4+} and I^{5+} sum energies associated with bound I_2^+ products. The intensity in the region with KE above 85 eV (marked on the top right) is scaled by a factor of 2 in order to better show the region corresponding to I_2^+ being formed at shorter bond lengths. **b** Normalized projections of the data in **a** for $0 < \tau < 200$ fs (black) and 600 fs $< \tau < 850$ fs (red). The error bars were calculated using the Poisson distribution. The black dash-dotted line marks the mean value of the static (“probe-only”)**

experimental distribution. The shaded areas depict the simulated sum KED for an I-I separation of 2.58 Å (magenta) and 3.60 Å (green). The simulated distributions are normalized such that their respective maxima match the experimental data.

c Delay-dependent mean value of the I^{4+} and I^{5+} sum KE, derived from the data above the white dashed line in **a**. The error bars reflect the standard error of the mean. The data are fitted with the sum of an error function and a sinusoidal function with 250 fs period. The right axis shows the internuclear separations of the formed I_2^+ product for which our simulations yield the mean values of the I^{4+} and I^{5+} sum KEs shown on the left axis.

fragments, assuming that the CH_2 group is far away, and its influence is negligible. The simulation was performed for the equilibrium I-I distances in the I_2^+ ground electronic state (2.58 Å^{44,45}, displayed in magenta in Fig. 3b) and in ground-state CH_2I_2 molecules (3.60 Å, displayed in green in Fig. 3b). The comparison between the experimental and simulated KEDs suggests that the range of I-I separations in the formed molecular products spans more than 1 Å. Notably, the I-I separation for many of the resulting I_2^+ is very close to that in the ground-state CH_2I_2 , which highlights the difficulty to detect this product with diffraction-based techniques.

To characterize the reaction products in more detail, we plot the mean value of the I^{4+} and I^{5+} sum KE as a function of delay in Fig. 3c. To eliminate contributions from three-body dissociation and decaying metastable states, we restrict this analysis to sum KEs >40 eV (white dashed horizontal line in Fig. 3a). Both the initial decrease of the energy and the build-up of the high-energy shoulder discussed above can be clearly observed in this graph. Furthermore, a pronounced oscillatory structure with a period of 250 ± 10 fs is visible in Fig. 3c for delays >200 fs. At this time, the methylene group is well separated from the iodines, such that the observed oscillation cannot be related to vibrations of the parent molecule (reflected by the 300-fs oscillation in Fig. 2d). We thus attribute this feature to the vibrational motion of the diatomic reaction product. The observed oscillation period and KED match the vibrational timescale and internuclear distance range (2.6 – 3.8 Å) expected for the $A^2\Pi_{u,3/2}$ electronic state of I_2^+ ⁴⁶. Therefore, our results suggest that this state (or, potentially, the $a^4\Sigma_u^-$ state,

which has very similar geometry) constitutes a significant fraction of the I_2^+ population produced by the NIR pump pulse. However, since the oscillating mean value of the experimental KED in Fig. 3c at large delays matches the simulations for 3.4 – 3.5 Å, above the equilibrium distance of the $A^2\Pi_{u,3/2}$ state (~ 3.1 Å^{44–46}), our results indicate that some higher-lying states are also populated.

So far, we have not explicitly addressed the reaction mechanism. All earlier studies of I_2 or I_2^+ elimination from CH_2I_2 ^{9–13,15,16,19} reported a dominance of concerted elimination, which is consistent with our results. Within the concerted elimination picture, the so-called synchronous and “asynchronous” reaction scenarios have been considered, corresponding to symmetric and asymmetric CH_2I_2 geometries at the time of I_2 formation^{9–13,15,16}. The first time-resolved study⁹ proposed the co-existence of synchronous and asynchronous mechanisms, while later works suggested that the asynchronous mechanism is dominant for I_2 formation in the highly excited neutral states^{10,12,13,16}. For I_2^+ formation, only the synchronous mechanism has been explicitly discussed^{15,19}.

In our molecular dynamics simulations (Fig. 4a–d), we find exemplary trajectories matching both scenarios. The first pathway (Fig. 4a, b) can be associated with the previously suggested synchronous mechanism, characterized by a simultaneous elongation of the two C-I bonds, accompanied by a decrease of the I-I distance when forming I_2^+ . Based on our calculations (Fig. 4b, d, and Supplementary Fig. 9b), the distance between the two iodine atoms decreases because the minimum of the ground- and excited-state potential energy curves

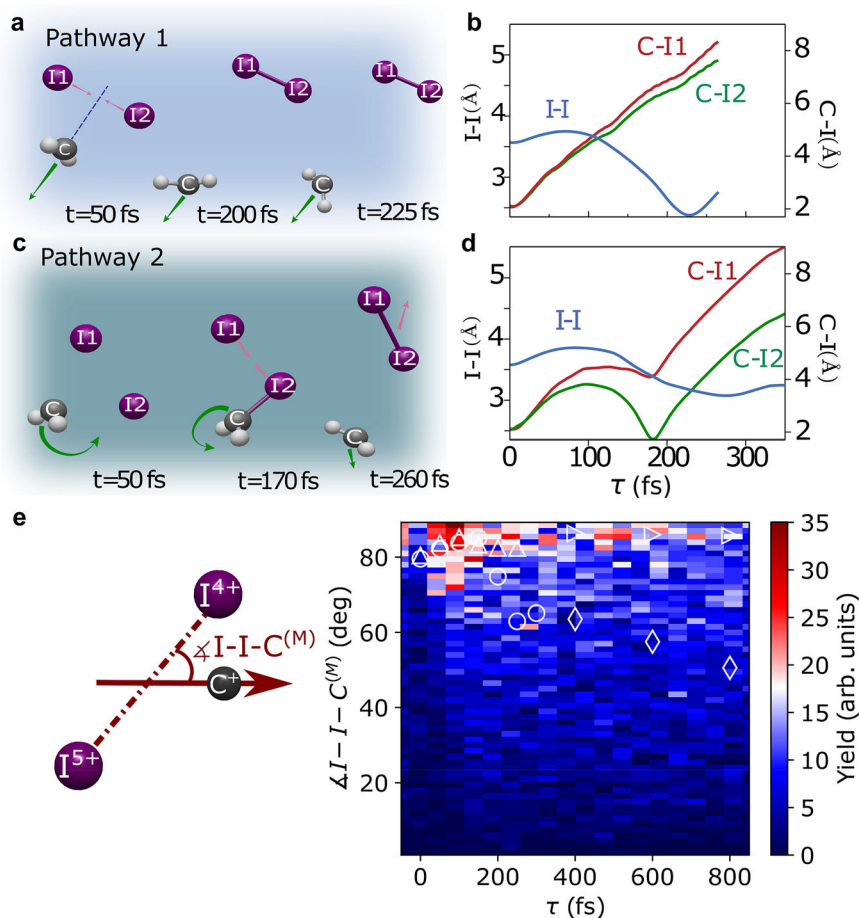


Fig. 4 | Simulated dynamics during I_2^+ formation from $CH_2I_2^+$ and the experimental distribution of the angle $\Delta I-I-C^{(M)}$. **a, c** Snapshots of the molecular structure at different time delays for two representative trajectories leading to I_2^+ formation. **b, d** Time evolution of C-I and I-I pair distances for the two trajectories illustrated in (a) and (c). **e** Sketch of the momentum-space angle $\Delta I-I-C^{(M)}$ and its experimental delay-dependent distribution. The up-pointing white triangles and

circles show the results of the Coulomb explosion simulations based on the simulated trajectories of (b) and (d), respectively. The right-pointing triangles and diamonds reflect the Coulomb explosion simulations at later time delays, for which the CH_2 fragment is assumed to be flying along the initial molecular symmetry axis (corresponding to pathway 1), or at 55° relative to the initial molecular symmetry axis (corresponding to pathway 2), respectively.

corresponding to I_2^+ formation is located at I-I distances shorter than the I-I distance in a neutral CH_2I_2 molecule. The CH_2 group moves away in a direction close to the molecular symmetry axis, while the iodine atoms approach each other. In the second pathway (Fig. 4c, d), after the initial cleavage of both C-I bonds, the CH_2 fragment bounces back to one of the iodine atoms (here I2), re-forming the C-I bond and passing through an “iso”-configuration^{27,28,47}, which corresponds to a local minimum in the $CH_2 + I_2^+$ potential energy curve (PEC) in Supplementary Fig. 9b. The CH_2 group then rotates around I_2^+ until the C-I bond breaks again and the I-I bond forms. These dynamics are consistent with the asynchronous mechanism introduced in refs. 9–14. For both pathways, the change of the total bond energy during the I_2^+ formation is accounted for by the translational kinetic energies of the CH_2 and I_2^+ products after the dissociation as well as their internal excitations.

In order to characterize synchronous and asynchronous pathways in our experimental data, we analyze the angular correlation between the three fragments. The measured delay-dependent momentum-space angle between the two iodine ions and the C^+ momentum direction, denoted as $\Delta I-I-C^{(M)}$, is plotted in Fig. 4e, together with simulations corresponding to the trajectories in Fig. 4a–d. In this representation, the synchronous reaction pathway is expected to produce a nearly constant $\Delta I-I-C^{(M)}$ angle of -85° (up-pointing and right-pointing triangles), whereas the asynchronous scenario (circles and diamonds) leads to significantly smaller $\Delta I-I-C^{(M)}$ values after the first

150 fs. The experimental data displays a broad $\Delta I-I-C^{(M)}$ distribution, which means that the iodine molecule is formed in a rather broad range of relative angles, supporting the co-existence of the two mechanisms. Moreover, the measured delay-dependent angular distribution shows a smooth decrease towards smaller $\Delta I-I-C^{(M)}$ values, suggesting that for the excitation scheme used in this study, there is no sharp distinction between the synchronous and asynchronous scenarios, and the reaction likely proceeds via a broad range of angular configurations.

In conclusion, we have experimentally mapped a light-induced elimination reaction involving correlated three-body dynamics unfolding on a femtosecond timescale and traced the motion of individual molecular constituents involved in the breaking of two molecular bond and the formation of a new one. While this reaction only results in approximately 10% of the total products generated by the NIR-molecule interaction, its signature could be isolated from all competing channels by exploiting the immense information content of coincident CEI as well as the reaction-pathway selectivity of the detected ion charge state combinations. Our model of X-ray ionization and fragmentation was benchmarked by imaging a bound vibrational wave packet and applied to characterize distinct three-body configurations leading to molecular iodine formation with different bond distances. We also imaged the vibrational motion of the formed products, facilitating the identification of their electronic states. With the several orders of magnitude increase in the effective repetition rates of

XFEL facilities planned for the near future, we expect the approach demonstrated here to become applicable to larger targets and more complex reactions.

Methods

Experimental setup

The experiment was performed using the COLTRIMS reaction microscope^{37,38} at the SQS instrument at the European XFEL. The experimental configuration and data sorting procedures were similar to those used in refs. 34,35. A supersonic gas jet was formed by sending helium gas (200 mbar) through a stainless-steel vessel containing liquid CH₂I₂ at room temperature and expanding the produced gas mixture through a 60 μm nozzle. The jet was further collimated with three skimmers and a set of adjustable slits, until it reached the interaction region located about 74 cm away from the nozzle. The ionic fragments from the interaction were extracted by a 400 V/cm electric field along the spectrometer (18 cm in length) to a time- and position-sensitive microchannel-plate detector (120 mm in diameter) with hexagonal delay-line position readout. Digitized detector signals were recorded by the data acquisition system along with shot-to-shot information about the X-ray pulse parameters and the NIR/X-ray pump-probe delay. The ions generated in each X-ray pulse were measured in coincidence. For each detected ion, the laboratory-frame 3D momentum vector was calculated from the measured time-of-flight (TOF) and hit position on the detector.

X-ray pulse properties and optical laser

The European XFEL operates in a burst mode, at a base repetition rate of 10 pulse trains per second. In the present experiment, we received in total 580 X-ray pulses per second, with an intra-train repetition rate of 188 kHz. The central photon energy of the XFEL pulse was 2 keV. The single-shot X-ray pulse energy (1 mJ on average) was measured upstream of the beamline mirrors by a gas monitor detector. The beamline transmission is about 80% at 2 keV⁴⁸. The X-ray pulses were focused in the F1 focus point of SQS by a pair of bendable Kirkpatrick-Baez mirrors. The focal spot size, which we chose to expand from the typical value of 1–2 μm in this focal point, was not measured directly but was estimated to be approximately 10 μm by comparing the measured charge-state distributions with simulations. The estimated upper limit of the X-ray pulse duration based on the electron bunch charge of 250 pC in the accelerator is 25 fs (FWHM). However, we carried out dedicated tuning of the undulator settings with feedback from the SASE3 grating spectrometer before the data taking, which suggests significantly shorter pulse durations based on spectral analysis⁴⁹ for the present experiment.

The optical laser was operated at the same repetition rate as the FEL, but the timing of the optical pulse train was offset from the X-ray pulse train, such that the first four laser pulses arrived before the X-ray burst, and the last four X-ray pulses arrived after the NIR laser pulse train. This provides a laser-only and X-ray-only background measurement in every pulse train. The NIR laser pulse duration was 15 fs (FWHM in intensity), and the maximum pulse energy available in the reaction chamber was 0.34 mJ. The laser beam was focused to the center of the interaction region with a spot size of 75 μm. For the experiment described here, the peak intensity of the NIR pulse was set to -1×10^{14} W/cm².

X-ray/laser timing and drift correction

The relative timing between the X-ray and optical laser pulses was monitored using an NIR/X-ray cross correlator installed downstream of the experiment, which used a second NIR beam path propagated collinearly to the main beam. This NIR beam was focused about 1 m downstream of the X-ray focus to a spot of ~300 μm on a diamond sample with a thickness of 100 μm. The X-ray-induced changes of the reflectivity of the diamond were encoded in the NIR spectra, which

were recorded at a repetition rate of 47 kHz (i.e., for every fourth laser pulse) using a Basler Racer line camera. In addition, electron bunch arrival monitors⁵⁰ were used to monitor drifts in the X-ray arrival time, and the arrival time jitter was corrected using this on a shot-by-shot basis for the following data analysis. The absolute time zero for the pump-probe measurement was determined with the help of a delay-dependent “step-function” feature in the low-energy He⁺ ion yield from the carrier gas, which is enhanced at negative delays due to NIR ionization of He atoms that were previously excited by the XFEL pulse. The slow timing drift between experimental runs (~1 h) was corrected by determining the center of the He⁺ “step-function” feature for each individual run and shifting the delay values accordingly. The corrections obtained with this approach agree with the simultaneous NIR/X-ray cross-correlation measurement.

The ultimate time resolution of the experiment, determined by the duration of both pulses and the remaining timing jitter, could be estimated from the cross correlation of the NIR and XFEL pulses obtained from the above-mentioned “step-function” feature in the delay-dependent yield of low-energy He⁺ ions. The error-function fit of this feature yielded the FWHM of 26 ± 7 fs, consistent with the sub-25 fs XFEL pulse duration mentioned above.

Excluding possible contamination from molecular dimers

Since the supersonic expansion in a molecular beam often leads to formation of molecular dimers and small molecular clusters, whose contributions can influence the experimental data for reaction channels with a small yield, such as the I₂ formation channel in the present experiment, it is important to make sure that the contamination from CH₂I₂ dimers or small clusters is negligible for the present data. Unambiguous signatures of dimer or cluster formation include the occurrence of dimer cations in the time-of-flight mass spectrum and of singly charged molecular parent ions with significant kinetic energy, which they would have acquired during Coulomb explosion of a dimer. Both signatures are undiscernible in our data (see Supplementary Fig. 3), suggesting that dimers were not formed above the background level. More importantly, any possible events related to the Coulomb explosion of dimers or clusters are excluded from the coincidence data because the momentum conservation condition applied during the coincidence analysis is only fulfilled if *all* fragment ions resulting from a monomer are detected in coincidence. Any fivefold coincidence event resulting from the Coulomb explosion of a dimer or cluster could not fulfil the momentum conservation condition and would be rejected.

Molecular-frame momentum distributions

The interaction events detected in the experiment were first sorted into different ion coincidence channels according to the charge states of the carbon and iodine ions. For each channel, we defined the molecular frame such that the carbon ion was emitted along the positive *x*-axis and the lower-charged of the two iodine ions was emitted within the *x*-*y* plane (*y* > 0). For channels such as C²⁺/I³⁺/I³⁺ that have equally charged iodine ions, one of the two was randomly chosen for the coordinate-frame definition. The molecular-frame momentum distributions (MFMDs) were then produced by transforming the momentum vectors of all ions within each interaction event from the laboratory frame to the above-defined molecular frame. Only those events that, in addition to carbon and iodine ions, contained at least one proton were included for the plots in Figs. 1–4.

Electronic structure calculations for simulating NIR-induced molecular dynamics

Ab initio multireference electronic structure calculations were performed based on state-averaged CASSCF wavefunctions, to characterize the ground and excited states of the diiodomethane cation. The active space in the CASSCF calculations contains 11 electrons in 8

orbitals (two lone pairs of each iodine atom, σ -Cl-bonding and σ^* -Cl-antibonding), and we averaged over 20 doublets and 9 quadruplets. The energy was corrected by perturbation theory in its extended multi-state CASPT2 (XMS-CASPT2) formalism⁵¹ with an imaginary shift of 0.2 and an IPEA shift of 0. The selection of the number of states included in the calculation correctly describes the dissociation limits of the different fragmentation channels: $\text{CH}_2\text{I}^+ + \text{I}^2(\text{P}_{3/2})$, $\text{CH}_2\text{I}^+ + \text{I}^2(\text{P}_{2})$, $\text{CH}_2\text{I}^+ + \text{I}^2(\text{P}_{1/2})$, $\text{CH}_2\text{I} + \text{I}^+(\text{P}_0)$, $\text{CH}_2\text{I} + \text{I}^+(\text{P}_1)$, $\text{CH}_2 + \text{I}_2^+$, and $\text{CH}_2^+ + \text{I}_2$. Relativistic effects were included in two steps. Firstly, one-electron integrals were modified using the Douglas-Kroll (DK) Hamiltonian^{52,53} in combination with the ANO-RCC^{54,55} contracted to a double zeta polarized (ANO-RCC-VDZP) basis set. Secondly, spin-orbit couplings (SOCs) were included with the restrictive active space interaction RASSI⁵⁶ and the atomic mean field integral AMFI⁵⁷ formalisms, resulting in a total of 76 states. All calculations were performed using the OpenMolcas code⁵⁸. The accuracy of the method was checked by computing the electronic energies following the minimal energy path between the neutral CH_2I_2 equilibrium geometry and the well-separated fragments: $\text{CH}_2\text{I}^+ (\text{CH}_2\text{I})/\text{I}^+ (\text{I}^+)$ and $\text{CH}_2 (\text{CH}_2^+)/\text{I}_2^+ (\text{I}_2)$. The nudged elastic band (NEB) technique^{59,60} was employed by using the FIRE algorithm as optimizer⁶¹ as implemented in Atomic Simulation Environment (ASE)^{62,63}. The required gradients and energies, i.e., the CASSCF ground electronic state with doublet multiplicity, were passed to the ASE code through an in-house interface with OpenMolcas⁵⁸. This method allows us to find the minimum energy path for the two fragmentation pathways. The energy of each intermediate structure was then recalculated with XMS-CASPT2 including the SOC as described before.

Simulations of NIR-induced molecular dynamics

To mimic the wave packet at time zero, a set of initial geometries and velocities was sampled by considering the Hessian of an MP2 optimization around the equilibrium geometry of the neutral CH_2I_2 and using a harmonic oscillator Wigner distribution in Cartesian coordinates with an open source code⁶⁴. We performed trajectory surface hopping dynamics using the SHARC method⁶⁵, where the Hamiltonian and the spin-free gradients were calculated numerically using the previously described electronic structure methodology (in XMS-CASPT2). A velocity-Verlet algorithm with a nuclear time step of 0.5 fs and a local diabaticization formalism⁶⁶ was used. The surface-hopping probabilities between states were evaluated using the flux formalism proposed by Petersen and Mitric⁶⁷. An energy-based decoherence correction was used with a parameter of 0.1 hartree⁶⁸. For describing the bound state I-C-I bending dynamics, the initial state is the ground doublet state. To study the NIR-induced dynamics leading to I_2^+ formation and $\text{CH}_2\text{I}^+/\text{I}^+ (\text{CH}_2\text{I}/\text{I}^+)$ dissociation, we chose our initial state with the energy well above (~ 15 eV) the $\text{CH}_2 + \text{I}_2^+$ dissociation limit to ensure our trajectories have enough energy to follow that fragmentation pathway.

Modeling of the interaction between X-rays and molecules and Coulomb explosion simulations

To model the X-ray-induced Coulomb explosion process, we used a theoretical model that combines Monte Carlo/Molecular Dynamics simulations (MC/MD)⁶⁹ with a classical over-the-barrier model⁷⁰⁻⁷² to track inner-shell Auger-Meitner cascades, redistribution of electrons in valence orbitals, and nuclear motion of fragments. X-ray absorption and inner-shell cascade processes are tracked by a Monte Carlo method, which determines the quantum electron transition probabilities of all participating electronic configurations (ECs), including ground state, core-excited states, and valence-excited states of all charge states. The electronic structure theory is based on the relativistic Hartree-Fock-Slater (HFS) method. The bound-state and continuum wavefunctions from the HFS method are used to compute the cross sections of photoionization, shake-off, electron-impact ionization, and electron-ion recombination processes as well as the decay

rates of Auger-Meitner and fluorescence decay processes in all participating ECs. The molecular dynamics method tracks the dynamics of atoms, ions, and delocalized ionized electrons.

A classical over-the-barrier (COB)⁷⁰⁻⁷² model simulates electron transfer dynamics in the valence shell. In this model, an electron fills a vacancy in the valence shell of a neighboring atom when its binding energy is higher than the Coulomb barrier. When the atoms are far apart, the resulting Coulomb barrier suppresses the electron transfer. In the original COB model, electron transfer takes place instantaneously when the electron orbital energy is higher than the Coulomb barrier. To go beyond this instantaneous model, which essentially yields either 0 or 1 for the electron transfer probability P_{ET} , we computed it at each time step (δt) of the simulations

$$P_{ET} = \gamma \delta t / t_{ET} \quad (1)$$

where γ is the electron transfer efficiency parameter, and t_{ET} is the electron transfer time, which is the time needed for the electron to travel the distance between the participating atom pair. The step size δt was set to 10 as for the first 100 fs, and 1 fs afterwards. The electron transfer efficiency γ was chosen to be 1.65×10^{-3} , which was obtained by optimizing the match between the simulated MFMD of the $\text{C}^{2+}/\text{I}^{3+}/\text{I}^{3+}$ channel with its experimental counterpart.

All Coulomb explosion simulations described in the following three subsections are based on this model. Its validity is independently verified by simulating the Coulomb explosion of the intact molecules (without the pump pulse), as shown in Supplementary Fig. 8. Furthermore, we tested our model by applying it to other channels, as illustrated in Fig. 2d and Supplementary Fig. 6, where the simulated I-C-I bending motion matches our experimental data remarkably well.

Time-dependent distribution of the momentum-space I-C-I angle $\Delta \text{IC}^{(M)}$

The time-dependent momentum-space angle $\Delta \text{IC}^{(M)}$ shown in Fig. 2d was obtained from the MFMD for the $\text{C}^{2+}/\text{I}^{3+}/\text{I}^{3+}$ channel. We first determined the $\Delta \text{IC}^{(M)}$ angle distribution at each NIR/X-ray delay τ , and then subtracted the $\Delta \text{IC}^{(M)}$ distribution produced from the XFEL-only run. The mean value of the resulting background-subtracted distribution is plotted as a function of the delay in Fig. 2d. For a more general mapping of the NIR-induced vibrational wave packet, in Supplementary Fig. 6a we combine the contributions from all channels dominated by the bound-state dynamics (labeled “I-C-I bending” in Supplementary Table 1a). We first repeated the procedure described above for each individual channel. In order to sum up different channels, they need to be scaled with respect to each other. This scaling was obtained by integrating all time delays for each channel, which yielded 1D Gaussian angular distributions. Using the extracted centers and widths of these Gaussians, we standardized the 2D distributions of each channel such that they all had the same centers and widths along the $\Delta \text{IC}^{(M)}$ axis as the $\text{C}^{2+}/\text{I}^{3+}/\text{I}^{3+}$ channel. The standardized distributions were then summed up to produce Supplementary Fig. 6a.

Coulomb explosion simulation of the momentum-space I-C-I angle $\Delta \text{IC}^{(M)}$

The initial position of each constituent atom was set according to the ground-state CH_2I_2 equilibrium geometry optimized with XMS-CASPT2/ ANO-RCC-VDZP (with 12 active electrons in 8 orbitals) and adjusted for different I-C-I angles $\Delta \text{IC}^{(R)}$. To create a mapping between the starting real-space angle $\Delta \text{IC}^{(R)}$ and the momentum-space I-C-I angle $\Delta \text{IC}^{(M)}$ of the final ion fragments, X-ray ionization simulations were performed at eight initial $\Delta \text{IC}^{(R)}$ angles ranging from 80° to 115° with a 5° spacing. Each simulation consisted of 432,000 Monte Carlo trajectories. At the end of each trajectory, the final charge state, position, velocity, and energy of the resulting atomic fragments were read out. Based on these outputs, we then constructed the molecular-

frame momentum distribution of the ion fragments in the $C^{2+}/I^{3+}/I^{3+}$ channel, from which the momentum-space I-C-I angle $\angle IC I^{(M)}$ is derived. By repeating this procedure for all simulations starting from different $\angle IC I^{(R)}$ angles, a mapping between the real-space and momentum-space angles is established (see Supplementary Fig. 2b). The simulated curves in Fig. 2d and Supplementary Fig. 6a were produced by converting the real-space oscillation obtained with the molecular dynamics simulation into fragment momentum space through the simulated correspondence shown in Supplementary Fig. 2b.

Coulomb explosion simulation of I_2^+ formation

Coulomb explosion simulations were carried out for both pathways of I_2^+ formation discussed in the paper. The pre-explosion molecular geometries at different time delays up to 350 fs were taken from the two exemplary trajectories shown in Fig. 4b, d. For the simulation at later time delays, the CH_2 fragment was assumed to fly along the initial molecular symmetry axis for pathway 1, and at 55° relative to the symmetry axis for pathway 2. The initial velocity of I_2^+ was determined by the centroid (0.06 eV) of the KED of I_2^+ produced with the optical laser only, which is plotted in Supplementary Fig. 4d. The velocity of the neutral CH_2 fragment was then obtained through momentum conservation. The two fragments move apart with these derived initial velocities until the X-ray pulse arrives at a certain delay τ . For the simulation of the relative angles of the final fragments, τ was chosen to be 0, 50, 100, 150, 200, 400, 600, and 800 fs. At each of these delays, X-ray ionization of the two fragments was simulated with 216,000 Monte Carlo trajectories, from which the final velocities and energies of the atomic fragments in the $C^+/I^{4+}/I^{5+}$ channel were produced. The KE and $\angle I-I-C^{(M)}$ angle displayed in Figs. 3b and 4e were then calculated based on these values. The bond length of the formed I_2^+ for these simulations was set to be 3.60 Å (2.58 Å was only used for the simulation in Fig. 2b), which is found to best match the experimental data for all simulations related to I_2^+ formation.

Data availability

The raw data recorded for the experiment at the European XFEL are available at <https://doi.org/10.22003/XFEL.EU-DATA-002676-00>. Further data that support the findings of this study are available from the corresponding authors upon request.

Code availability

The code for the molecular dynamics simulations is available at <https://doi.org/10.5281/zenodo.7352971> and <https://github.com/Molcas/OpenMolcas>. The code for the calculations of the X-ray–molecule interaction is available from the corresponding authors upon request.

References

1. Elimination Reactions. JoVe Core in Organic Chemistry, Journal of Visualized Experiments. <https://app.jove.com/science-education/v/11756/elimination-reactions> (2021).
2. Biggs, B. A. & Ogilvie, W. W. Eliminations to form alkenes, allenes, and alkynes and related reactions. *Compr. Org. Synth.* **6**, 802–841 (2014).
3. Ouellette, R. J. & Rawn, J. D. Haloalkanes and alcohols: introduction to nucleophilic substitution and elimination reactions. *Org. Chem. Study Guide* **9**, 135–167 (2015).
4. Zewail, A. H. Femtochemistry: atomic-scale dynamics of the chemical bond. *J. Phys. Chem. A* **104**, 5660–5694 (2000).
5. Dantus, M., Bowman, R. M. & Zewail, A. H. Femtosecond laser observations of molecular vibration and rotation. *Nature* **343**, 737–739 (1990).
6. Kim, S. K., Pedersen, S. & Zewail, A. H. Direct femtosecond observation of the transient intermediate in the α -cleavage reaction of $(CH_3)_2CO$ to $2CH_3+CO$: resolving the issue of concertedness. *J. Chem. Phys.* **103**, 477–480 (1995).
7. Ihee, H. et al. Direct imaging of transient molecular structures with ultrafast diffraction. *Science* **291**, 458–462 (2001).
8. Lee, J. H. et al. Capturing transient structures in the elimination reaction of haloalkane in solution by transient X-ray diffraction. *J. Am. Chem. Soc.* **130**, 5834–5835 (2008).
9. Marvet, U. & Dantus, M. Femtosecond observation of a concerted chemical reaction. *Chem. Phys. Lett.* **256**, 57–62 (1996).
10. Zhang, Q., Marvet, U. & Dantus, M. Concerted elimination dynamics from highly excited states. *Faraday Discuss* **108**, 63–80 (1997).
11. Marvet, U., Zhang, Q., Brown, E. J. & Dantus, M. Femtosecond dynamics of photoinduced molecular detachment from halogenated alkanes. I. Transition state dynamics and product channel coherence. *J. Chem. Phys.* **109**, 4415–4427 (1998).
12. Zhang, Q., Marvet, U. & Dantus, M. Femtosecond dynamics of photoinduced molecular detachment from halogenated alkanes. II. Asynchronous concerted elimination of I_2 from CH_2I_2 . *J. Chem. Phys.* **109**, 4428–4442 (1998).
13. Marvet, U., Zhang, Q. & Dantus, M. Femtosecond dynamics of unimolecular and unrestricted bimolecular reactions. *J. Phys. Chem. A* **102**, 4111–4117 (1998).
14. Marvet, U., Brown, E. J. & Dantus, M. Femtosecond concerted elimination of halogen molecules from halogenated alkanes. *Phys. Chem. Chem. Phys.* **2**, 885–891 (2000).
15. Liu, Z. H., Wang, Y.-Q., Ma, J.-J., Wang, L. & He, G.-Z. Concerted elimination of CH_2I_2 and CH_2ICl under intense femtosecond laser excitation. *Chem. Phys. Lett.* **383**, 198–202 (2004).
16. Chen, S.-Y. et al. I_2 molecular elimination in single-photon dissociation of CH_2I_2 at 248 nm by using cavity ring-down absorption spectroscopy. *J. Chem. Phys.* **134**, 034315 (2011).
17. Okabe, H., Kawasaki, M. & Tanaka, Y. The photodissociation of CH_2I_2 : Production of electronically excited I_2 . *J. Chem. Phys.* **73**, 6162–6166 (1980).
18. Baughcum, S. L. & Leone, S. R. Photofragmentation infrared emission studies of vibrationally excited free radicals CH_3 and CH_2I . *J. Chem. Phys.* **72**, 6531–6545 (1980).
19. Geißler, D., Pearson, B. J. & Weinacht, T. Wave packet driven dissociation and concerted elimination in CH_2I_2 . *J. Chem. Phys.* **127**, 204305 (2007).
20. Wei, Z. et al. Ultrafast dissociative ionization and large-amplitude vibrational wave packet dynamics of strong-field-ionized diiodomethane. *J. Chem. Phys.* **151**, 214308 (2019).
21. O'Dowd, C. D. et al. Marine aerosol formation from biogenic iodine emissions. *Nature* **417**, 632–636 (2002).
22. Saiz-Lopez, A. et al. Atmospheric chemistry of iodine. *Chem. Rev.* **112**, 1773–1804 (2012).
23. Centurion, M., Wolf, T. J. A. & Yang, J. Ultrafast Imaging of Molecules with Electron Diffraction. *Annu. Rev. Phys. Chem.* **73**, 21–42 (2022).
24. Liu, Y. et al. Spectroscopic and structural probing of excited-state molecular dynamics with time-resolved photoelectron spectroscopy and ultrafast electron diffraction. *Phys. Rev. X* **10**, 021016 (2020).
25. Odate, A., Kirrander, A., Weber, P. M. & Miniti, M. P. Brighter, faster, stronger: ultrafast scattering of free molecules. *Adv. Phys. X* **8**, 2126796 (2023).
26. Horton, S. L. et al. Excited-state dynamics of CH_2I_2 and CH_2BrI studied with UV pump VUV probe photoelectron spectroscopy. *J. Chem. Phys.* **150**, 174201 (2019).
27. Park, S. et al. Fate of transient isomer of CH_2I_2 : Mechanism and origin of ionic photoproducts formation unveiled by time-resolved x-ray liquidography. *J. Chem. Phys.* **150**, 224201 (2019).
28. Panman, M. R. et al. Observing the structural evolution in the photodissociation of diiodomethane with femtosecond solution X-ray scattering. *Phys. Rev. Lett.* **125**, 226001 (2020).
29. Rebholz, M. et al. All-XUV pump-probe transient absorption spectroscopy of the structural molecular dynamics of diiodomethane. *Phys. Rev. X* **11**, 031001 (2021).

30. Fukuzawa, H. et al. Real-time observation of X-ray-induced intramolecular and interatomic electronic decay in CH₂I₂. *Nat. Commun.* **10**, 2186 (2019).
31. Liu, Y., Rozgonyi, T., Marquetand, P. & Weinacht, T. Excited-state dynamics of CH₂I₂ and CH₂BrI studied with UV-pump VUV-probe momentum-resolved photoion spectroscopy. *J. Chem. Phys.* **153**, 184304 (2020).
32. Vager, Z., Naaman, R. & Kanter, E. P. Coulomb explosion imaging of small molecules. *Science* **244**, 426–431 (1989).
33. Pitzer, M. et al. Direct determination of absolute molecular stereochemistry in gas phase by Coulomb explosion imaging. *Science* **341**, 1096–1100 (2013).
34. Boll, R. et al. X-ray multiphoton-induced Coulomb explosion images complex single molecules. *Nat. Phys.* **18**, 423–428 (2022).
35. Li, X. et al. Coulomb explosion imaging of small polyatomic molecules with ultrashort X-ray pulses. *Phys. Rev. Res.* **4**, 013029 (2022).
36. Kim, J. G. et al. Mapping the emergence of molecular vibrations mediating bond formation. *Nature* **582**, 520–524 (2020).
37. Dörner, R. et al. Cold Target Recoil Ion Momentum Spectroscopy: a ‘momentum microscope’ to view atomic collision dynamics. *Phys. Rep.* **330**, 95–192 (2000).
38. Ullrich, J., Moshhammer, R., Dorn, A., Dörner, R., Schmidt, L.P.H. & Schmidt-Böcking, H. Recoil-ion and electron momentum spectroscopy: reaction-microscopes. *Rep. Prog. Phys.* **66**, 1463–1545 (2003).
39. Crane, S. W., Lee, J. W. L., Ashfold, M. N. R. & Rolles, D. Molecular photodissociation dynamics revealed by Coulomb explosion imaging. *Phys. Chem. Chem. Phys.* **25**, 16672–16698 (2023).
40. Erk, B. et al. Imaging charge transfer in iodomethane upon X-ray photoabsorption. *Science* **345**, 288–291 (2014).
41. Hansen, J. L. et al. Control and femtosecond time-resolved imaging of torsion in a chiral molecule. *J. Chem. Phys.* **136**, 204310 (2012).
42. Christensen, L. et al. Dynamic stark control of torsional motion by a pair of laser pulses. *Phys. Rev. Lett.* **113**, 073005 (2014).
43. Schnorr, K. XUV Pump-Probe Experiments on Electron Rearrangement and Interatomic Coulombic Decay in Diatomic Molecules. PhD Thesis, University of Heidelberg (2014).
44. de Jong, W. A., Visscher, L. & Nieuwpoort, W. C. Relativistic and correlated calculations on the ground, excited, and ionized states of iodine. *J. Chem. Phys.* **107**, 9046–9058 (1997).
45. Li, J. & Balasubramanian, K. Spectroscopic properties and potential energy curves of I₂ and I₂⁺. *J. Mol. Spectrosc.* **138**, 162–180 (1989).
46. Fang, L. & Gibson, G. N. Investigating excited electronic states of I₂⁺ and I₂²⁺ produced by strong-field ionization using vibrational wave packets. *Phys. Rev. A* **75**, 063410 (2007).
47. Borin, V. A., Matveev, S. M., Budkina, D. S., El-Khoury, P. Z. & Tarnovsky, A. N. Direct photoisomerization of CH₂I₂ vs. CHBr₃ in the gas phase: a joint 50 fs experimental and multireference resonance-theoretical study. *Phys. Chem. Chem. Phys.* **18**, 28883–28892 (2016).
48. Baumann, T. M. et al. Harmonic radiation contribution and X-ray transmission at the Small Quantum Systems instrument of European XFEL. *J. Synchrotron Rad.* **30**, 662–670 (2023).
49. Serkez, S. et al. Wigner distribution of self-amplified spontaneous emission free-electron laser pulses and extracting its autocorrelation. *J. Synchrotron. Rad.* **28**, 3–17 (2021).
50. Viti, M. et al. FLASH and European XFEL. In *Proceedings of the 16th International Conference on Accelerator and Large Experimental Control Systems ICALEPCS2017*. (JACoW, Geneva, Switzerland, 2017).
51. Shiozaki, T., Györfy, W., Celani, P. & Werner, H.-J. Communication: Extended multi-state complete active space second-order perturbation theory: Energy and nuclear gradients. *J. Chem. Phys.* **135**, 081106 (2011).
52. Reiher, M. & Wolf, A. Exact decoupling of the Dirac Hamiltonian. I. General theory. *J. Chem. Phys.* **121**, 2037–2047 (2004).
53. Reiher, M. & Wolf, A. Exact decoupling of the Dirac Hamiltonian. II. The generalized Douglas–Kroll–Hess transformation up to arbitrary order. *J. Chem. Phys.* **121**, 10945–10956 (2004).
54. Widmark, P.-O., Malmqvist, P.-Å & Roos, B. O. Density matrix averaged atomic natural orbital (ANO) basis sets for correlated molecular wave functions. *Theor. Chim. Acta* **77**, 291–306 (1990).
55. Roos, B. O., Lindh, R., Malmqvist, P.-Å, Veryazov, V. & Widmark, P.-O. Main group atoms and dimers studied with a new relativistic ANO basis set. *J. Phys. Chem. A* **108**, 2851–2858 (2004).
56. Malmqvist, P.-Å, Roos, B. O. & Schimmelpfennig, B. The restricted active space (RAS) state interaction approach with spin-orbit coupling. *Chem. Phys. Lett.* **357**, 230–240 (2002).
57. Schimmelpfennig, B. AMFI, an atomic mean-field spin-orbit integral program. University of Stockholm (1996).
58. Li Manni, G. et al. The OpenMolcas Web: a community-driven approach to advancing computational chemistry. *J. Chem. Theory Comput.* **19**, 6933–6991 (2023).
59. Berne, B. J., Cicciotti, G. & Coker, D. F. *Classical and Quantum Dynamics in Condensed Phase Simulations*. (World Scientific, 1998).
60. Henkelman, G., Uberuaga, B. P. & Jónsson, H. A climbing image nudged elastic band method for finding saddle points and minimum energy paths. *J. Chem. Phys.* **113**, 9901–9904 (2000).
61. Bitzek, E., Koskinen, P., Gähler, F., Moseler, M. & Gumbusch, P. Structural relaxation made simple. *Phys. Rev. Lett.* **97**, 170201 (2006).
62. Larsen, A. H. et al. The atomic simulation environment—a Python library for working with atoms. *J. Phys: Condens. Matter* **29**, 273002 (2017).
63. Bahn, S. R. & Jacobsen, K. W. An object-oriented scripting interface to a legacy electronic structure code. *Comput. Sci. Eng.* **4**, 56–66 (2002).
64. González-Vázquez, J. *Generator of Initial Conditions* (2019).
65. Richter, M., Marquetand, P., González-Vázquez, J., Sola, I. & González, L. SHARC: *ab initio* molecular dynamics with surface hopping in the adiabatic representation including arbitrary couplings. *J. Chem. Theory Comput.* **7**, 1253–1258 (2011).
66. Plasser, F. et al. Surface hopping dynamics using a locally diabatic formalism: Charge transfer in the ethylene dimer cation and excited state dynamics in the 2-pyridone dimer. *J. Chem. Phys.* **137**, 22A514 (2012).
67. Petersen, J. & Mitrić, R. Electronic coherence within the semiclassical field-induced surface hopping method: strong field quantum control in K₂. *Phys. Chem. Chem. Phys.* **14**, 8299–8306 (2012).
68. Granucci, G. & Persico, M. Critical appraisal of the fewest switches algorithm for surface hopping. *J. Chem. Phys.* **126**, 134114 (2007).
69. Ho, P. J. & Knight, C. Large-scale atomistic calculations of clusters in intense X-ray pulses. *J. Phys. B: At. Mol. Opt. Phys.* **50**, 104003 (2017).
70. Ryufuku, H., Sasaki, K. & Watanabe, T. Oscillatory behavior of charge transfer cross sections as a function of the charge of projectiles in low-energy collisions. *Phys. Rev. A* **21**, 745 (1980).
71. Niehaus, A. A classical model for multiple-electron capture in slow collisions of highly charged ions with atoms. *J. Phys. B: At. Mol. Opt. Phys.* **19**, 2925 (1986).
72. Schnorr, K. et al. Electron rearrangement dynamics in dissociating I₂ⁿ⁺ molecules accessed by extreme ultraviolet pump-probe experiments. *Phys. Rev. Lett.* **113**, 073001 (2014).

Acknowledgements

We acknowledge the European XFEL in Schenefeld, Germany, for the provision of X-ray free-electron laser beam time at the SQS instrument and thank the EuXFEL staff for their assistance. K.B., B.K., H.V.S.L., E.W., D.R., and A.R. were supported by the US Department of Energy, Office of Science, Office of Basic Energy Sciences, Chemical Sciences, Geosciences, and Biosciences Division under contract no. DE-FG02-86ER13491. S.B. and K.C. were supported by contract no. DE-

SC0020276, and P.J.H. was supported by the contract no. DE-AC02-06CH11357 from the same funding agency. X.L., R.F. and J.P.C. are supported by the Linac Coherent Light Source (LCLS), SLAC National Accelerator Laboratory, which is funded by the U.S. Department of Energy, Office of Science, Office of Basic Energy Sciences under Contract No. DE-AC02-76SF00515. A.S.V. was funded through the National Science Foundation (NSF) grant No. PHYS1753324 and, during the final phase of the project, grant No. PHYS-2409365. P.V.Z. is funded through the National Science Foundation (NSF) grants Nos. CHE-2054616 and CHE-2054604 and is grateful to the Simons Foundation for the computational resources used in this research. J.G.V. thanks the projects PID2022-138288NB-C32 and PID2019-106732GB-I00 funded by MCIN/AEI/10.13039/501100011033 and the European Union “NextGenerationEU”/PRTRMICINN programs. A.G. was supported by the European Union Marie Curie project 101067645. F.T. acknowledges funding by the Deutsche Forschungsgemeinschaft (DFG, German Research Foundation) - Project 509471550, Emmy Noether Program. M.I. was partly supported by the Bundesministerium für Bildung und Forschung (BMBF) under grant 13K22CHA. M.M. acknowledges support by the Cluster of Excellence ‘Advanced Imaging of Matter’ of the DFG—EXC 2056 and project ID 390715994.

Author contributions

A.R. conceived the experiment, which was carried out by X.L., R.B., D.Ri., S.B., K.B., K.C., A.D.F., B.E., R.F., A.G., M.I., E.K., H.V.S.L., T.Ma., T.Mu., B.S., F.T., S.U., A.S.V., E.W., M.M., T.J., D.Ro. and A.R. X.L. analyzed the data, with the help of S.B., K.B., K.C., A.G., B.K., E.K., H.V.S.L., A.S.V., J.P.C., E.W. and T.J. B.K., D.Ro. and A.R. conducted preliminary NIR-only measurements. P.V.Z. carried out the molecular dynamics calculations with the help of J.G.V. P.J.H. and X.L. carried out the X-ray ionization calculations. X.L., R.B., P.V.Z., P.J.H., D.Ro., and A.R. interpreted the results and wrote the paper with input from all authors.

Competing interests

The authors declare no competing interests.

Additional information

Supplementary information The online version contains supplementary material available at <https://doi.org/10.1038/s41467-025-62274-z>.

Correspondence and requests for materials should be addressed to Xiang Li or Artem Rudenko.

Peer review information *Nature Communications* thanks the anonymous reviewer(s) for their contribution to the peer review of this work. A peer review file is available.

Reprints and permissions information is available at <http://www.nature.com/reprints>

Publisher’s note Springer Nature remains neutral with regard to jurisdictional claims in published maps and institutional affiliations.

Open Access This article is licensed under a Creative Commons Attribution-NonCommercial-NoDerivatives 4.0 International License, which permits any non-commercial use, sharing, distribution and reproduction in any medium or format, as long as you give appropriate credit to the original author(s) and the source, provide a link to the Creative Commons licence, and indicate if you modified the licensed material. You do not have permission under this licence to share adapted material derived from this article or parts of it. The images or other third party material in this article are included in the article’s Creative Commons licence, unless indicated otherwise in a credit line to the material. If material is not included in the article’s Creative Commons licence and your intended use is not permitted by statutory regulation or exceeds the permitted use, you will need to obtain permission directly from the copyright holder. To view a copy of this licence, visit <http://creativecommons.org/licenses/by-nc-nd/4.0/>.

© The Author(s) 2025